JOURNAL OF GUIDANCE, CONTROL, AND DYNAMICS
Vol. 32, No. 3, May–June 2009

Aeroassisted Orbital Transfer Trajectory Optimization Considering Thermal Protection System Mass

Christian Gogu,* Taiki Matsumura,† Raphael T. Haftka,‡ and Anil V. Rao§
University of Florida, Gainesville, Florida 32611

DOI: 10.2514/1.37684

Aeroassisted orbital transfer is recognized as a potential technology to enhance operational responsiveness in space with significant fuel savings. To endure aerodynamic heating resulting from the flight through the atmosphere, however, considerable thermal protection is required, thereby potentially decreasing the mass savings due to lower fuel consumption. In this paper, the relationship between achievable fuel savings and thermal protection system size is investigated by coupling trajectory optimization and thermal protection system design through the single parameter of maximum heating rate constraint. The optimal solution that minimizes the total mass of fuel and the thermal protection system is then determined. A trajectory optimization procedure and a thermal protection system mass estimation model are then applied to the transfer of a vehicle between two low-Earth orbits with a specified inclination change. All trajectory parameters, including deorbit, boost, and recircularization impulses, are optimized and the thermal protection system is sized with ablative and reusable materials. It is found that the minimum overall mass (fuel and thermal protection system) is achieved when no heating rate constraint is imposed, which is also the scenario that minimizes the fuel consumption alone.

Nomenclature

C_D	=	coefficient of drag
C_{D0}	=	zero-lift coefficient of drag
C_L	=	coefficient of lift
$C_{L,\alpha}$	=	derivative of C_L with respect to α
$C_{L,\max}$	=	maximum coefficient of lift
D	=	drag acceleration
g	=	gravitational acceleration
g_0	=	gravitational acceleration at sea level
h_a	=	heat of ablation
h_{atm}	=	altitude of sensible atmosphere
h_v	=	heat of vaporization
h_0	=	altitude of low-Earth orbit
I_{sp}	=	specific impulse
i	=	inclination
i_d	=	desired inclination change
i_e	=	inclination at exit of atmospheric flight
J	=	performance index
K	=	drag polar parameter
L	=	lift acceleration
m	=	vehicle mass
m_{abl}	=	mass of ablative thermal protection system material
m_e	=	vehicle empty mass
m_{end}	=	vehicle mass at the end of the mission (after recircularization)
m_f	=	mass of initial fuel
m_{reu}	=	mass of reusable thermal protection system material
m_0	=	vehicle gross mass
$Q_{\text{abl,ave}}$	=	average total heat load of ablative section
$Q_{\text{abl,max}}$	=	maximum total heat load of ablative section (heat load at stagnation point)
$Q_{\text{reu,ave}}$	=	average total heat load in reusable thermal protection system section
$Q_{\text{reu,max}}$	=	maximum total heat load in reusable thermal protection system section
Q_A	=	ablation heat load
Q_C	=	conduction heat load
$\dot{Q}$	=	heating rate
$\dot{Q}_c$	=	conduction heating rate
$\dot{Q}_{\text{limit}}$	=	maximum operational heating rate limit for reusable material
$\dot{Q}_{\max}$	=	maximum stagnation point heating rate
q	=	dynamic pressure
q_A	=	heat of ablation
$\dot{q}_c$	=	heating rate to keep thermal protection system surface at its ablation temperature
R_E	=	radius of Earth
r	=	radius
r_e	=	radius at exit of atmospheric flight
S	=	vehicle reference area
S_{abl}	=	area of ablative section
S_{reu}	=	area of reusable section
$T_{\text{abl,max}}$	=	maximum thickness of ablative thermal protection system material
$T_{\text{reu,max}}$	=	maximum thickness of reusable thermal protection system material
t	=	time
u_1, u_2	=	control variables
v	=	velocity
v_e	=	velocity at exit of atmospheric flight
v_E	=	circular orbit speed at surface of the Earth
v_0	=	circular orbit speed at low-Earth orbit
α	=	angle of attack
γ	=	flight-path angle
γ_e	=	flight-path angle at exit of atmospheric flight
ΔV_1	=	magnitude of impulse for deorbit
ΔV_2	=	magnitude of impulse to raise the apogee of the transfer orbit
ΔV_3	=	magnitude of impulse for recircularization

Presented as Paper 898 at the 2008 Aerospace Sciences Meeting, Reno, NV, 7–10 January 2008; received 23 March 2008; revision received 2 December 2008; accepted for publication 3 December 2008.

*Graduate Research Assistant, Department of Mechanical and Aerospace Engineering, Post Office Box 116250. Student Member AIAA.

†Visiting Researcher; currently Deputy Manager, Space Transportation Mission Directorate, Japan Aerospace Exploration Agency.

‡Distinguished Professor, Department of Mechanical and Aerospace Engineering, Post Office Box 116250. Fellow AIAA.

§Assistant Professor, Department of Mechanical and Aerospace Engineering, Post Office Box 116250; anilvrao@ufl.edu. (Corresponding Author)

δ = recession thickness of ablative thermal protection system material
θ = longitude angle
μ = gravitational parameter
ρ = air density
ρ_{abl} = density of ablative material
ρ_E = air density at sea level
ρ_{reu} = density of reusable material
σ = bank angle
ϕ = latitude angle
ψ = heading angle

I. Introduction

VEHICLES such as the Orbital Space Plane (OSP) have been recognized in recent years as concepts that greatly increase operational responsiveness in space [1]. In particular, an OSP-type vehicle can potentially provide both efficient regular transportation and safe return of crew members in case of an emergency in orbit (e.g., catastrophic failure of life support systems of the International Space Station). To improve operational responsiveness, it is useful for the OSP to have high cross-range capability during atmospheric flight (i.e., the OSP must be capable of aeroassisted orbital transfer). In addition to improving the reachable footprint, aeroassisted technology potentially enhances an on-orbit maneuver, such as orbital transfer and orbital plane change, and lowers its fuel consumption, thereby reducing overall mission cost as compared to an all-propulsive orbital transfer.

The idea of aeroassisted orbital transfer has been studied extensively in the literature and much of the early work is summarized in [2,3]. More recently, optimal trajectories that are subject to high heating rate constraints have been studied. The difference in flight profile between aerocruise with propulsive maneuver and aeroglide without propulsive maneuver is shown in [4]. The minimum energy-loss trajectory of an aeroglide maneuver with various heating rate constraints is presented in [5]. Also, Zimmermann and Calise [6] evaluated the maximum inclination change of aerocruise under the various heating limits. In addition, multiple-pass aeroassisted orbital transfer from geostationary orbit to low-Earth orbit with desired inclination change, subject to heating rate constraints, was studied in [7,8]. Finally, the somewhat more practical Pienkowski et al. [9] studied the feasibility of multiple-pass aeroassisted orbital transfer with inclination change for the X-37 vehicle.

Heating considerations are of utmost importance in aeroassisted orbital transfer because the fuel consumption of the transfer is negatively correlated with the vehicle's ability to withstand heating during atmospheric flight (i.e., the higher the heat resistance of the vehicle, the lower the fuel consumption). On the other hand, the heat rate profile (and thus the integrated heat load) directly determines the thickness and mass of the vehicle's thermal protection system. From the standpoint of vehicle system design, the simultaneous trajectory and thermal protection system (TPS) design can be treated as a multidisciplinary design optimization (MDO) problem.

In this study, the simultaneous trajectory optimization and TPS design is investigated to determine the minimum mass of a high lift-to-drag (L/D) ratio aeroassisted orbital transfer vehicle (AOTV) for a problem with orbital plane change. The desired inclination change is accomplished using an aeroglide (i.e., nonthrusting) maneuver during atmospheric flight. The trajectory optimization and the TPS design are coupled through a single coupling parameter, the maximum heating rate constraint. Also, by fixing the total mass, fuel, and exterior shape of the vehicle, a reverse coupling from TPS sizing is eliminated from the problem. That is, we assume that any variations in the TPS or fuel savings will change payload size and mass. The assumption of fixed mass and shape is reasonable when we design the AOTV that will be launched by a launch vehicle. Actually, such a vehicle has a fixed payload capacity and the payload shape is constrained by the rocket nose fairing. It is also assumed that no other coupling between the trajectory and TPS design, other than the heating rate constraint, exists. By using these assumptions, we can solve the MDO problem sequentially. These simplifying assumptions allow one to greatly reduce the computational cost of the MDO problem. Indeed, TPS sizing is computationally expensive and the computational cost would become prohibitive if the TPS would be sized at each step of the trajectory optimization. Constructing a surrogate model of the TPS mass could be an alternative for reducing computational cost. Note, however, that the surrogate model would have to depend on a high number of variables, which complicates its construction.

This paper is organized as follows. The MDO framework with single coupling parameter is given in Sec. II. The methods of the trajectory optimization and TPS sizing are described in Secs. III and IV, respectively. Section V provides the results obtained for the MDO problem. Finally, in Sec. VI, we provide concluding remarks.

II. Design Framework with Single Coupling Parameter

Past studies (see [4–8]) have shown that the allowable maximum heating rate is a key parameter in determining the inclination change capability of an AOTV, because the available aerodynamic force is limited by heat resistance capability. When the AOTV has the capability to withstand high heating, it can fly deeper in the atmosphere and benefit from a large aerodynamic force due to the denser atmosphere, which provides the vehicle with a larger and quicker inclination change. Also, Rao et al. [7] showed that the heating rate constraint has a significant effect on fuel saving performance of an AOTV mission. On the other hand, TPS has to be sized to resist a given heating condition. We deal with the heating rate constraint as a coupling parameter that connects the trajectory optimization and the TPS design.

Although it may be evident that the trajectory impacts TPS design, it may be less intuitive that a reverse coupling exists as well, that is, that the TPS design impacts the trajectory due to the fact that changes in the TPS size and shape change the mass and shape of the vehicle. Consequently, these changes would have an effect on aerodynamic parameters, such as L/D, and center of gravity of the vehicle. By fixing the total mass, fuel, and exterior shape of the vehicle, this reverse coupling is eliminated from the problem. That is, we assume that any variations in the TPS or fuel savings will change payload size and mass. The assumption of fixed mass and shape is reasonable when we design the AOTV that will be launched by a launch vehicle. Indeed, such a vehicle has a fixed payload capacity and the AOTV shape is constrained by the rocket nose fairing. It is also assumed that no other coupling between the trajectory and TPS design other than the heating rate constraint exists. By using these assumptions and the single coupling parameter, we can solve the MDO problem sequentially.

First, the optimal trajectory is determined that minimizes the fuel consumption to achieve the desired inclination change for various heating rate constraints. For each trajectory obtained, the size of the TPS is subsequently determined. Finally, we determine the optimum design by finding the heating rate corresponding to the minimum combined weight of the fuel and TPS. This design process is schematically described in Fig. 1.

The trajectory optimization problem is posed as a nonlinear optimal control problem and is solved using the software GPOCS [10], which is an implementation of the Gauss pseudospectral method [11]. For the second step relative to the thermal shield design, the TPS sizing is carried out using both ablative and reusable materials. To calculate the required thickness of the TPS, we use a simplified analysis tool called "the virtual ablation method" [12] for the ablative material and a finite element heat-transfer analysis for the reusable material. We chose to use a partly ablative TPS instead of an all-reusable TPS (with different reusable materials according to the vehicle portion) because initial results have shown that, for heat rate constraints compatible with all-reusable TPS, aeroassisted orbital transfer cannot achieve fuel savings with respect to an all-propulsive maneuver. We show later that a heat rate constraint of about 300 W/cm^2 is the absolute minimum to achieve weight savings for the AOT maneuver considered in this study.

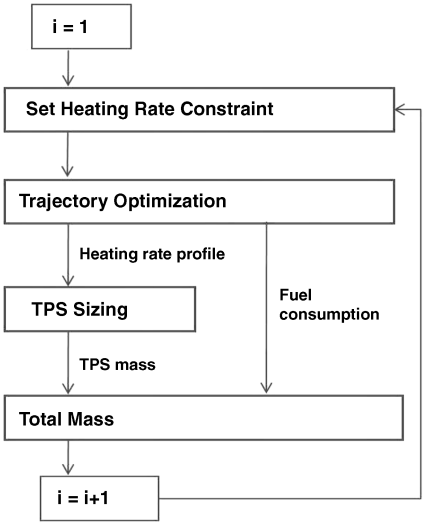

Fig. 1 Design framework of AOTV with fixed size and total mass.

III. Trajectory Optimization for Aeroassisted Orbital Transfer

The orbital transfer problem considered is the following. The transfer is started with a deorbit impulse from an initial circular low-Earth orbit (LEO) with altitude h_0 resulting in an elliptic transfer orbit. The initial LEO and the elliptic orbit are assumed to lie in the equatorial plane. The elliptic transfer orbit terminates at an altitude h_{atm}, where h_{atm} is the altitude at the edge of the sensible atmosphere (i.e., the altitude at which the atmosphere is first sensible by onboard instrumentation). The vehicle then flies with aerodynamic control through the atmosphere under the influence of drag, lift, and gravity such that the atmospheric flight segment terminates at an altitude of h_{atm}. Upon atmospheric exit, a second impulse is applied to raise the apogee of the resulting transfer orbit. After the application of the second impulse, the vehicle flies along another elliptic transfer orbit until apogee is attained. Upon reaching apogee, a third impulse is applied to recircularize the orbit. The event sequence for the trajectory optimization is given as

$$\text{deorbit impulse} \longrightarrow \text{Keplerian flight} \longrightarrow \text{atmospheric flight} \longrightarrow \text{boost impulse} \longrightarrow \text{Keplerian flight} \longrightarrow \text{Circularization impulse}$$

Finally, a schematic of the orbital transfer corresponding to the trajectory event sequence is shown in Fig. 2.

A. Physical and Vehicle Models

For this study, the vehicle is modeled as a point mass in motion over a spherical nonrotating Earth.[¶] During exoatmospheric flight, the vehicle is assumed to be solely under the influence of spherical gravity, with the exception of three specific instants of time where impulsive thrust is applied. The first impulse ΔV_1 is applied from the initial circular orbit of radius $r_0 = h_0 + R_E$ (where R_E is the radius of the Earth), thereby resulting in an elliptic transfer orbit that intersects the sensible atmosphere. The directions of ΔV_1 is determined via Euler pitch angle η and Euler yaw angle χ. The Euler angles are measured in a velocity reference frame as shown in Fig. 3. The vehicle mass at the atmospheric flight m is calculated as

$$m = m_0 \exp(-\Delta V_1 / g_0 I_{\text{sp}}) \tag{1}$$

In this paper, we first solve the case where all inclination change is achieved purely by the aerodynamic force during atmospheric flight (i.e., $\eta = 180$ deg and $\chi = 0$ deg). Then we calculate the case where the propulsive inclination change at deorbit is allowed. In this case η is fixed at 180 deg and the magnitude of ΔV_1 and χ are optimized.

The second impulse ΔV_2 is applied upon exit from the atmosphere where the radius, speed, and flight-path angle are given, respectively, as r_e, v_e, and γ_e. The second impulse raises the apogee of the ascending elliptical orbit to the initial LEO radius r_0. After atmospheric exit (i.e., right after ΔV_2 is applied and before ΔV_3 is applied), it is known that the energy and angular momentum are conserved. As a result, ΔV_2 is given as

$$\Delta V_2 = \left[\frac{2\mu(1/r_e - 1/r_0)}{1 - (r_e/r_0)^2 \cos^2\gamma_e}\right]^{1/2} - v_e \tag{2}$$

Similarly, the third impulse ΔV_3 is applied at the apogee of the postatmospheric space flight segment to recircularize the elliptical orbit to a radius of r_0 (where the circular orbit speed is v_0). The third impulse is then obtained as

$$\Delta V_3 = v_0 - \frac{r_e}{r_0}\left[\frac{2\mu(1/r_e - 1/r_0)}{1 - (r_e/r_0)^2 \cos^2\gamma_e}\right]^{1/2} \cos\gamma_e \tag{3}$$

During atmospheric flight, the vehicle is assumed to be under the influence of drag, lift, and gravity. The 3-degree-of-freedom differential equations of motion are given in spherical coordinates [13] as

$$\frac{\mathrm{d}r}{\mathrm{d}t} = v\sin\gamma \tag{4}$$

$$\frac{\mathrm{d}\theta}{\mathrm{d}t} = \frac{v\cos\gamma\cos\psi}{r\cos\phi} \tag{5}$$

$$\frac{\mathrm{d}\phi}{\mathrm{d}t} = \frac{v\cos\gamma\sin\psi}{r} \tag{6}$$

$$\frac{\mathrm{d}v}{\mathrm{d}t} = -D - g\sin\gamma \tag{7}$$

$$\frac{\mathrm{d}\gamma}{\mathrm{d}t} = \frac{1}{v}\left[L\cos\sigma - \left(g - \frac{v^2}{r}\right)\cos\gamma\right] \tag{8}$$

$$\frac{\mathrm{d}\psi}{\mathrm{d}t} = \frac{1}{v}\left[\frac{L\sin\sigma}{\cos\gamma} - \frac{v^2}{r}\cos\gamma\cos\psi\tan\phi\right] \tag{9}$$

Next, the magnitude of the gravitational acceleration is given as

$$g = \mu/r^2 \tag{10}$$

The lift and drag accelerations are given, respectively, as

$$D = qSC_D/m \tag{11}$$

$$L = qSC_L/m \tag{12}$$

where $q = \rho v^2/2$ is the dynamic pressure. The atmospheric density is calculated from a 1962 U.S. Standard Atmosphere model [14]. The aerodynamic model used in this study is a drag polar of the form

$$C_L = C_{L,\alpha}\alpha \tag{13}$$

$$C_D = C_{D0} + KC_L^2 \tag{14}$$

It is assumed in this study that the vehicle is lift-limited such that $C_L \in [0, C_{L,\max}]$. The aerodynamic and physical model of the high

[¶]It is noted that the results of this study will be somewhat different, but qualitatively similar, if a rotating planet were considered.

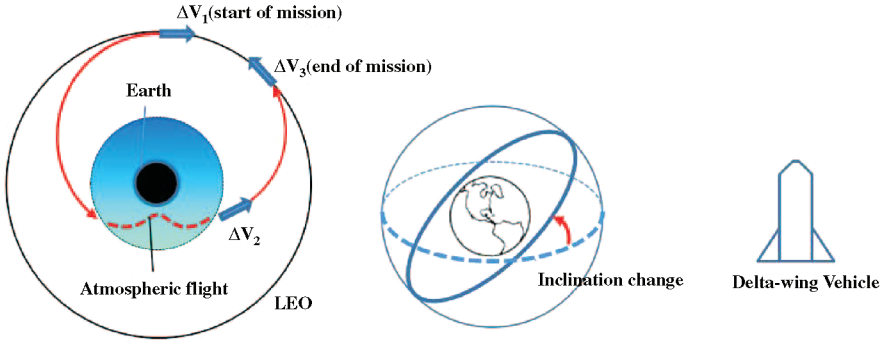

Fig. 2 Schematic of mission scenario of AOTV along with vehicle shape.

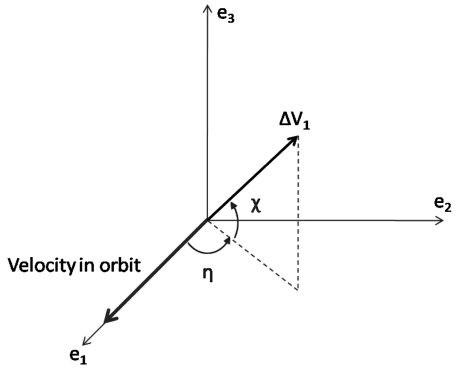

Fig. 3 Definition of deorbit impulse ΔV_1.

L/D delta-wing vehicle and the numerical values of all constants used in this study are adapted from [6] and shown in Table 1. The corresponding orbital inclination is given by

$$\cos i = \cos\phi \cos\psi \tag{15}$$

B. Path Constraints and Boundary Conditions

During atmospheric flight, the following path constraints (taken from [7]) are imposed on the vehicle. First, an inequality path constraint on the stagnation point heating rate $\dot{Q}$ is imposed. The model for the stagnation point heating rate is taken from [15] and is given as

$$\dot{Q} = \dot{\bar{Q}}\left(\frac{\rho}{\rho_E}\right)^{1/2}\left(\frac{v}{v_E}\right)^{3.15} \tag{16}$$

Table 1 Aerodynamic data, vehicle data, and physical data of AOTV Problem

Quantity		Numerical value
m_0	Vehicle gross mass	4898.7 kg
m_e	Vehicle empty mass	2195.9 kg
m_f	Vehicle fuel mass	2702.8 kg
R_E	Radius of Earth	6378.4 km
μ	Gravitational parameter	398,970 km^2/s^2
S	Vehicle reference area	11.69 m^2
C_{D0}	Zero-lift coefficient of drag	0.032
K	Drag polar parameter	1.4
$C_{L,\alpha}$	Derivative of C_L with respect to α	0.5699
$C_{L,\max}$	Maximum coefficient of lift	0.4
$L/D_{\max}$	Maximum lift-to-drag ratio	2.36
h_0	Initial LEO altitude	185.2 km
h_{atm}	Altitude of sensible atmosphere	129.6 km
I_{sp}	Specific impulse	310 s
$\dot{\bar{Q}}$	Heating rate constant	19,987.44 W/m^2

where $\dot{\bar{Q}}$ is a constant for which the numerical value is given in Table 1. Note that this model accounts only for convective heating. To simplify the model, we neglect the radiative heating contribution in this study. The heating rate constraint is then given as

$$\dot{Q} \le \dot{Q}_{\max} \tag{17}$$

Next, because of aliasing problems associated with using the bank angle, the following controls are used in place of the angle of attack and bank angle, meaning that u_1 and u_2 are the control variables of this optimization problem:

$$u_1 = -C_L \sin\sigma \tag{18}$$

$$u_2 = -C_L \cos\sigma \tag{19}$$

Then, in terms of u_1 and u_2, we have

$$C_L = \sqrt{u_1^2 + u_2^2} \tag{20}$$

The following inequality path constraint is then imposed on u_1 and u_2 during atmospheric flight:

$$\sqrt{u_1^2 + u_2^2} \le C_{L,\max} \tag{21}$$

Next, to ensure that the vehicle can reach apogee after exiting the atmosphere, the flight-path angle must be positive at atmospheric exit, that is,

$$\gamma_e \ge 0 \tag{22}$$

Also, the mission goal is to achieve the desired inclination change i_d. Consequently, the following boundary-condition constraint is applied at the atmospheric exit:

$$i_e = i_d \tag{23}$$

C. Objective Function

To get the optimal trajectory which minimizes the fuel consumption, the objective function is set to maximize the final vehicle mass m_{end}, subject to the path constraints and for a given final inclination change. The performance index is described as

$$J = -m_f \tag{24}$$

where m_f is the final vehicle mass after the recircularization to the initial LEO and obtained by calculating the fuel consumption of each impulse as

$$m_f = m_0 \exp(-\Delta V_1/g_0 I_{\text{sp}}) \exp(-\Delta V_2/g_0 I_{\text{sp}}) \exp(-\Delta V_3/g_0 I_{\text{sp}}) \tag{25}$$

D. Numerical Optimization

The aeroassisted orbital plane change problem is solved using the optimal control software GPOCS [10] which is an implementation of the Gauss pseudospectral method developed in [10]. In this study, a single-phase optimal control problem was posed using 50 nodes (i.e., 50 Legendre–Gauss points). GPOCS uses the TOMLAB [16] version of the sparse nonlinear programming solver SNOPT [17].

IV. Estimating Mass of Thermal Protection System

In our mission scenario, the vehicle will enter Earth's atmosphere at hypersonic speed and meet a severe heating environment. Some sections of the vehicle will experience very high heating rates requiring an ablative heat shield because reusable TPS materials have operational temperature limits. Ablative TPS materials accommodate high heating rates and heat loads through phase change and mass loss (i.e., pyrolysis, charring, and recession). However, ablative materials have a disadvantage in terms of mass because the densities of ablative materials are higher than those of reusable materials. We therefore apply an ablative TPS material in high heating environments and a reusable material in low heating environments. For the ablative material, we considered two flight-certified materials, SLA-561 and AVCOAT-5026-39H/CG [18]. SLA-561 was developed and used as an ablative heat shield on the Viking mission. SLA-561 has lower density and is composed of a silicone resin with cork, phenolic microballoon, silica microballoon, and refractory fiber fillers. AVCOAT-5026-39H/CG is an older material, used for the Apollo mission, but it is still considered a potential candidate for the TPS of the crew exploration vehicle. AVCOAT-5026-39H/CG consists of an epoxy-novalac resin reinforced with quartz fibers and phenolic microballoons. For the reusable material, we chose the LI-900 rigidized ceramic insulation tiles which are used over the major portion of the windward surface (bottom side) of the space shuttle orbiter. The material properties of these materials are taken from [12,19,20], and some of the relevant properties are shown in Table 2. Note that, in our models, we used temperature-dependent material properties for the thermal conductivity and specific heat. In the following section, we present the procedure to estimate mass of the TPS, which consists of TPS area definition, required thickness sizing, and total TPS mass calculation.

A. Selection of Thermal Protection System Materials According to Surface Location

The selection of TPS with ablative materials SLA-561 or AVCOAT-5026-39H/CG and reusable material LI-900 is made in the following manner. First, for a given AOTV trajectory, the peak heating rate is calculated at the nose stagnation point by Eq. (16). The variations of the heating rate along the windward streamline of the vehicle are modeled by the normalized heating rate distribution shown in Fig. 4, which was obtained on a generic space plane vehicle geometry [21] in an optimization study of a high L/D vehicle. Note that, to simplify the problem, the normalized heating rate distribution is assumed to be applied uniformly over the entire vehicle (not varying along the width of the vehicle) and not to vary with the angle of attack during the atmospheric flight. The heat rate distribution of Fig. 4 is for a laminar flow. During the atmospheric flight of reentry vehicles, such as the space shuttle, there is typically a transition to turbulent flow at lower altitudes. However, analysis based on space shuttle reentry data indicates that laminar conditions would prevail for the altitudes and speeds encountered during an aeroassisted orbital transfer trajectory. Accordingly, we assumed the AOTV to be subject to a purely laminar flow regime. If transition to the turbulent regime was included, this would reduce L/D, increase the TPS weight, thus reducing the advantage of an AOT maneuver over an all-propulsive plane change.

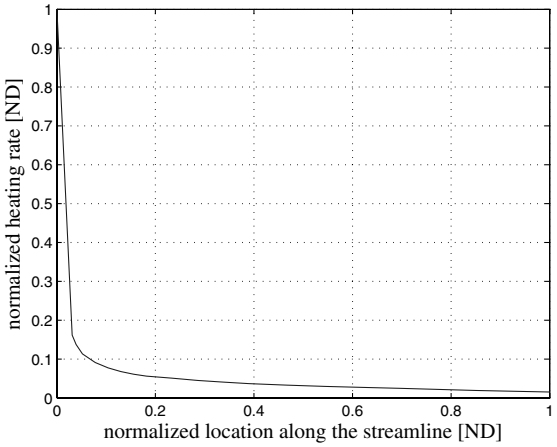

Fig. 4 The normalized heating rate distribution curve.

TPS materials are mapped to each surface location using an appropriate heating rate range for each TPS material. For the area where the heating rate is below the maximum operational heating rate of the reusable material $\dot{Q}_{\text{limit}}$, LI-900 is applied. For the area above

Table 3 Heating rate ranges for various materials

Heating rate ranges	Material selection
$\dot{Q} > \dot{Q}_{\text{limit}}$	Ablative material
$\dot{Q} \leq \dot{Q}_{\text{limit}}$	Reusable material (LI-900)
($\dot{Q}_{\text{limit}} = 31.9$ W/cm^2)	

Table 2 Material properties

Ablative material		
Material	Quantity	Numerical value
SLA-561	Heat of ablation	5.41×10^7 J/kg
	Density (virgin material)	2.64×10^2 kg/m^3
	Thermal conductivity @295 K [a]	5.92×10^{-2} W/mK
	Specific heat @295 K [a]	1.17×10^3 J/kgK
	Ablation temperature	922 K
AVCOAT-5026-39H/CG	Heat of ablation	1.38×10^7 J/kg
	Density (virgin material)	5.29×10^2 kg/m^3
	Thermal conductivity @295 K [a]	2.97×10^{-1} W/mK
	Specific heat @295 K [a]	1.70×10^3 J/kgK
	Ablation temperature	922 K
Reusable material		
Material	Quantity	Numerical value
LI-900	Density	1.442×10^2 kg/m^3
	Thermal conductivity @295 K [a]	4.76×10^{-2} W/mK
	Specific heat @295 K [a]	6.28×10^2 J/kgK
	Maximum operational temperature	1590 K

[a]Actual temperature-dependent material properties are used from [20].

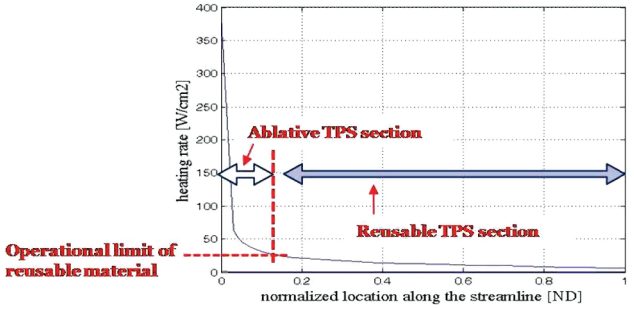

Fig. 5 Schematic of TPS area definition.

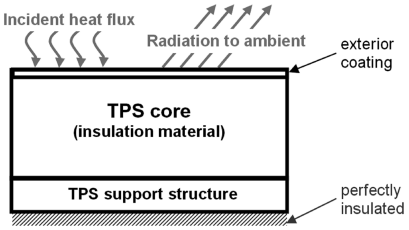

Fig. 6 Schematic representation of the thermal problem.

the operational heating limit, the ablative materials are applied. The concept of the material selection is drawn schematically in Fig. 5 and shown in Table 3. Using the radiative thermal equilibrium temperature, $\dot{Q}_{\text{limit}}$ for LI-900 is calculated as 31.9 W/cm^2.

The shape of the vehicle is assumed to be approximately similar to the X-37 vehicle. By using the vehicle length, width [22], and the geometric shape, we approximate the bottom surface area of X-37. Then, by using a ratio of reference areas, the bottom surface area of the vehicle is obtained as 42.5 m^2 [22].

B. Required Thermal Protection System Thickness Sizing

In this section, we determine the TPS thickness required for the positions of maximum heat load. For the ablative TPS section, this occurs for the stagnation heating rate profile, and for the reusable section, it occurs for the heating rate profile, peaking at the operational limit of the reusable material $\dot{Q}_{\text{limit}}$.

To determine the maximum TPS thickness of the LI-900 section, where the heating rate is at the operational limit of LI-900 $\dot{Q}_{\text{limit}}$, we used a transient finite element (FE) heat-transfer model. The heat-transfer problem is modeled as shown in Fig. 6.

The TPS is composed of the main core material (LI-900 in this case) which is usually covered by a thin exterior coating. This coating, reaction cured glass (RCG) in our case, acts mainly as an emissivity enhancing and oxidation protection layer. The core TPS material is also usually attached through a strain isolation pad to a TPS support structure. The TPS support structure is assumed to be perfectly insulated. The assumption of perfect insulation is a worst-case scenario because, if heat could leak through the support structure, the maximum temperature would decrease, thus becoming less critical. We assume an aluminum support structure 0.254-cm thick. This thickness is the one assumed in [23] which compares different TPS for reusable launch vehicles. In addition, the thickness value (typical for the TPS of such vehicles) is used in our parametric study. If a detailed structural model of the vehicle is available, the support structure thickness can of course be computed much more accurately. Note that this represents a homogenized thickness. In reality, we would have a thinner skin reinforced with stiffeners. The exterior TPS surface is subject to an incident heating rate and outgoing radiation. The incident heating rate is the stagnation point heating rate for the corresponding trajectory scaled down to $\dot{Q}_{\text{limit}}$ maximum. This problem is modeled as a one-dimensional transient finite element heat-transfer model using the commercial FE software Abaqus®. Fifty-four three-node heat-transfer link elements were used for the three sections of the TPS (exterior RCG coating, LI-900 TPS core, and aluminum support structure). Temperature-dependent material properties from the Material Properties Database of NASA, TPSX, [19] and [20] were used for all sections. After the end of the atmospheric heating, the simulation is continued with an additional time step, where only radiation is assumed at the top surface. This is because the maximum support structure temperature peaks well after the end of the atmospheric flight. The thickness of the LI-900 insulation required was sized using this FE model. Successive analyses were carried out with variable insulation thickness until the minimum thickness was found that allowed the maximum support structure temperature to be 450 K or less, which is the maximum operational temperature of aluminum.

To calculate the thickness of the ablative material at the stagnation point, we used a simplified analysis tool called the virtual ablation method [12]. The key concept of this method is to divide a total heat load into two components, as shown in Fig. 7. One is called the ablation heat load Q_A, which makes a contribution only to the ablation process. The other is the conduction heat load Q_C, which consists of the heat conducted into the TPS (accounting for the heat capacity of the TPS, the heat influx, and the heat radiated away from the surface). Each of these heat loads determines a certain thickness, the thickness of the ablated material and the thickness of the ablative insulation, respectively, as shown in Fig. 7. To apply this procedure, we need to determine the conduction heating rate profile, which would maintain the TPS surface at ablation temperature. To obtain the value of this heating rate $\dot{Q}_c$, we carried out repeated heat-transfer analyses using a FE model similar to that described previously for the reusable TPS section. For more details on the virtual ablation method, refer to [12].

To obtain the total ablative TPS thickness, add the insulation thickness required to maintain the support structure below the operational temperature limit (450 K) under the conduction heating

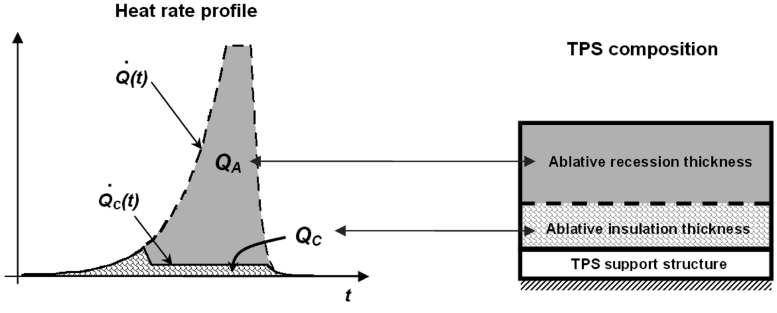

Fig. 7 Virtual ablation methods.

Table 4 Heat of ablation, h_a

Ablative material	Heat of ablation
SLA-561	1.43×10^{10} J/m^3
AVCOAT-5026-39H/CG	1.26×10^{10} J/m^3

rate $\dot{Q}_c$ to the thickness of the material that is ablated (i.e., the recession thickness, which is determined by Q_A (cf. Fig. 7). To determine the insulation thickness, we use the conduction heat load as input to a FE heat-transfer model similar to that used for the LI-900 TPS sizing. For the incident heating rate $\dot{Q}_c$, we iteratively determined the TPS thickness that keeps the support structure of the TPS under the operational temperature limit (450 K). Temperature-dependent material properties are used such that the properties of the char layer and those of the virgin layer are combined into a single material. We finally calculate the ablative recession layer thickness δ using the heat of vaporization h_v and the ablation heat load Q_A through Eq. (26):

$$\delta = \frac{Q_A}{h_v} \tag{26}$$

where h_v is calculated from the density of the material ρ_{abl} and the heat of ablation h_a (given in Table 4). The relationship between h_v, ρ_{abl}, and h_a is then given as

$$h_v = \rho_{\text{abl}} h_a \tag{27}$$

Note that, in the procedure we use to calculate the ablative insulation thickness, we assume that the recession layer does not provide insulation. This is a conservative assumption because the recession thickness for our application is high. Furthermore, the recession of ablative materials during the atmospheric flight might affect the aerodynamic characteristic such as L/D, however, for simplicity, as mentioned in Sec. II, we neglect this effect, assuming a constant L/D.

C. Total Thermal Protection System Mass Calculation

In the previous subsection, we calculated the TPS thicknesses at the maximum heat load points for each section. To calculate the mass of the entire TPS, we use the average thickness over the vehicle surface for each of the two TPS sections. This is done in the following way.

The recession thickness of the ablative TPS is proportional to the heat load [see Eq. (26)]. The thickness of the insulation part of the ablative TPS and the reusable material are calculated by the one-dimensional transient finite element heat-transfer model described in previous section. Figure 8 shows a plot of the required thickness of all the materials vs the conduction heat load (note that the curves for the ablative materials concern only the thickness that serves as insulation and not the one which is ablated, which explains why these curves span over the small heat load interval). From this plot, we can see that a linear approximation of thickness as a function of heat load would also suffice to determine the insulation thicknesses. This approximation allows us to calculate the average thickness over the vehicle very easily by using the average heat load over the vehicle.

For the ablative TPS section, we obtain the average thickness by multiplying the maximum thickness $T_{\text{abl,max}}$ by the ratio between the average heat load with respect to the streamline location of the ablative TPS section (obtained from Fig. 4) $Q_{\text{abl,ave}}$ and the maximum heat load (for which the maximum thickness was calculated) $Q_{\text{abl,max}}$. Finally, by multiplying the average thickness by the density ρ_{abl} and the area over which the ablative material is deployed S_{abl}, we can obtain the total mass of the ablative TPS over the vehicle m_{abl}, as in Eq. (28):

$$m_{\text{abl}} = T_{\text{abl,max}} \frac{Q_{\text{abl,ave}}}{Q_{\text{abl,max}}} \rho_{\text{abl}} S_{\text{abl}} \tag{28}$$

A similar approach is used for the LI-900 reusable material section. Using the maximum thickness of the LI-900 section $T_{\text{reu,max}}$, which corresponds to the stagnation point heating rate scaled down to $\dot{Q}_{\text{limit}}$ (the maximum heating rate for which LI-900 can still be used), we obtain the average thickness by multiplying by the ratio between the average heat load of the reusable TPS section (obtained from Fig. 4) $\rho_{\text{reu,ave}}$ and the maximum heat load (for which the maximum thickness was just calculated) $q_{\text{reu,max}}$. Multiplying by the density ρ_{reu} and the corresponding area S_{reu}, we obtain the LI-900 TPS mass m_{reu}, as shown in Eq. (29):

$$m_{\text{reu}} = T_{\text{reu,max}} \frac{Q_{\text{reu,ave}}}{Q_{\text{reu,max}}} \rho_{\text{reu}} S_{\text{reu}} \tag{29}$$

Finally, by adding the masses of the ablative section, the reusable section, and the support structure (aluminum), we can obtain the total TPS mass for the AOTV.

V. Results and Discussion

A. Trajectories of Aeroglide

The aeroassisted orbital plane change optimal control problem described in Sec. III was solved with $i_d = 18$ deg and $\dot{Q}_{\max} = (397, 454, 568, 681)$ W/cm^2 [$=(350, 400, 500, 600)$ Btu/ft$^2 \cdot$ s]. Figure 9 shows the altitude as a function of time. Additional details of the trajectory optimization results are provided in Appendix A.

We see in Fig. 9 that, with high heating rate constraints, the vehicle can dip deeper into the atmosphere and use the higher aerodynamic loads to stay in the atmosphere for a shorter time. This results in a smaller heat load, as shown in Fig. 10 and Table 5. Table 5 also shows the ΔVs and the fuel consumption for each heating rate constraint case. All cases require much less fuel than the all-propulsive maneuver, where the required ΔV is 2439.2 m/s and the corresponding fuel consumption is 2702.8 kg. For the aeroassisted

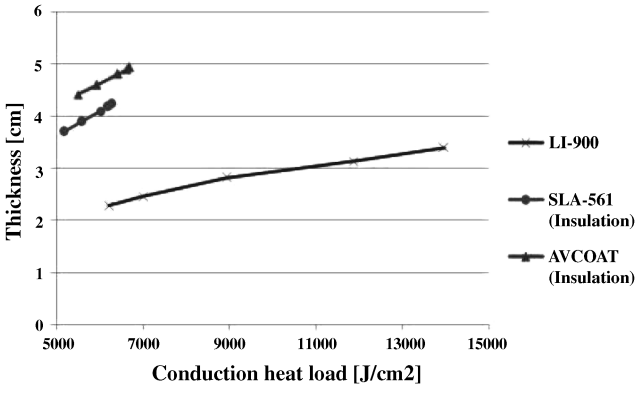

Fig. 8 Required TPS thickness vs conduction heat load.

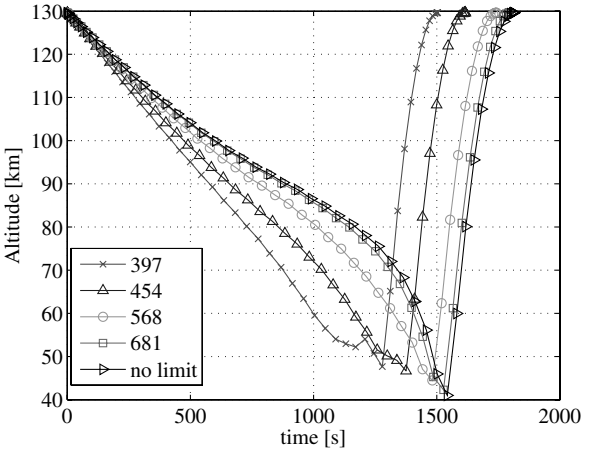

Fig. 9 Altitude vs time.

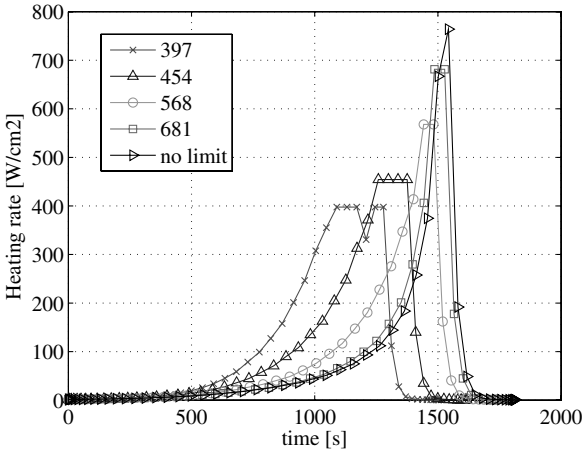

Fig. 10 Heating rate vs time.

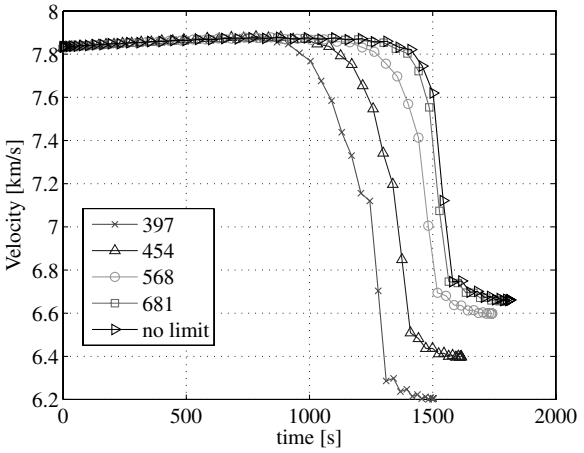

Fig. 11 Velocity vs time.

maneuvers, the fuel consumption increases for lower heating rate constraints. This is mainly caused by the difference in the magnitude of ΔV_2. As seen in Eq. (2), ΔV_2 mainly depends on the velocity at the exit of the atmosphere v_e and, in the most fuel consuming case, where the heating rate constraint is 397 $\mathrm{W/cm^2}$, it can be seen that the value of v_e is the smallest (Fig. 11). This is because, due to the low heating rate constraint, the vehicle has to fly longer through the dense atmosphere because the lateral aerodynamic force for the inclination change is limited, meaning that it is exposed longer to a high drag force. This increased duration of atmospheric flight reduces most of the velocity at atmospheric exit, which, in turn, results in the fuel consumption being the highest for the lowest heating rate.

An interesting feature in terms of TPS design is that, when the heating rate constraint is lowered, the total heat load, which is the key factor to determine the required TPS thickness, increases. This is related to the effect we mentioned earlier. When the heating rate is further constrained, the lateral aerodynamic force for the inclination change is limited, so that the vehicle has to fly longer at its maximum heating rate where the vehicle can generate the largest aerodynamic force (Fig. 10).

B. Thermal Protection System Mass Estimation

Table 6 shows the maximum heat load and the maximum thickness for the LI-900 section of the insulation. The lower the heating rate constraint, the thicker the maximum thickness of the LI-900 section corresponding to the total heat load.

The heat load distribution for the ablative TPS sizing is obtained as shown in Table 7, and the required maximum insulation thickness and the recession thickness for the ablative TPS section are given in Table 8. Similar to the total heat load, the ablative heat load increases as the heating rate constraint decreases. This results in the maximum recession thickness of ablative TPS getting thicker as the limit on heating rate gets lower. Comparing the SLA-561 and AVCOAT-5026-39H/CG sections, the insulation thickness of AVCOAT-5026-39H/CG is slightly thicker than that of the SLA-561, due mainly to the relatively high thermal conductivity of AVCOAT-5026-39H/CG. The recession layer thicknesses of both materials are similar because their heat of ablation is close to each other (see Table 4).

An interesting feature is that the recession thickness of the ablative section is larger than the required insulation, which can keep the support structure of the TPS under the operational temperature limit. This trend was not seen in past experience of reentry missions that used ablative materials for heat shielding, such as the Apollo mission and the Stardust mission. In these past missions, the recession thicknesses of the materials was small compared to the required thickness for heat shielding, that is, 4.8 cm total ablative TPS thickness with 1.2 cm of recession for the Stardust mission [24], and 0.9-in. thickness with about 0.1 in. of recession for the Apollo flight AS 202 [18,25]. The AOTV maneuver, however, lasts much longer than a typical reentry maneuver to achieve the required orbital plane change [compared to about 800 s with 22731 $\mathrm{J/cm^2}$ ($20,000$ $\mathrm{Btu/ft^2}$) for the Apollo mission [26] and about 80 s with $28,000$ $\mathrm{J/cm^2}$ for the Stardust mission [24]], thus making the recession thickness much larger, as explained later. Commonly, for a reentry mission, the ablative materials with a high temperature resistance and a low thermal diffusivity can block a sudden impact of high heating rate, so that its trajectory is designed to reduce the total heat load by taking the highest possible heating rate and shortening the mission time. The reduced total heat load mitigates the disadvantage of its high thermal conductivity which might cause excessive conduction heat transfer to the support structure. However, in the severe heating environment of the aeroassisted orbital plane change, where both the total heat load and the heating rate are quite high, it can be seen that the recession layer of the ablative material has to be quite large as well. The manufacturing limit of ablative material thickness is generally up to about 5–10 cm, and so creating the required ablative TPS thickness is one of the challenges of AOTV design.

The results for the area definition and mass estimation are given in Tables 9–11, respectively. The mass of the LI-900 varies corresponding to the maximum required thickness (i.e., the thicker the maximum thickness, the heavier the total LI-900 mass). For the

Table 6 Maximum heat load and maximum thickness of LI-900 TPS section

Constraints, $\mathrm{W/cm^2}$	No limit	681	568	454	397
Total heat load, $\mathrm{J/cm^2}$	6219	7004	8939	11,871	13,975
Thickness, cm	2.28	2.46	2.82	3.13	3.40

Table 5 Fuel consumption and heat load

$\dot{Q}_{\max}$, $\mathrm{W/cm^2}$	ΔV_1, m/s	ΔV_2, m/s	ΔV_3, ft/s	Fuel consumption, kg	Total heat load, $\mathrm{J/cm^2}$
397	35.8	1641.9	16.6	2088.9	174,070
454	32.9	1448.3	16.6	1901.8	168,987
568	30.3	1247.8	16.6	1695.3	159,006
681	28.9	1189.6	16.6	1632.1	149,559
No limit	28.7	1185.5	16.6	1627.6	148,915
All-propulsive case		2439.2		2702.8	0

Table 7 Heat load distribution for ablative TPS sizing

Constraints, W/cm^2		No limit	681	568	454	397
	Total heat load, J/cm^2	148,915	149,559	159,006	168,987	174,070
SLA-561	Ablation heat load, J/cm^2	142,639	143,350	152,979	163,408	168,896
$\dot{Q}_c = 3.81$ W/cm^2	Conduction heat load, J/cm^2	6576	6209	6027	5579	5174
AVCOAT-5026	Ablation heat load, J/cm^2	142,223	142,940	152,589	163,054	168,570
$\dot{Q}_c = 4.02$ W/cm^2	Conduction heat load, J/cm^2	6692	6619	6417	5933	5500

Table 8 Maximum thickness of ablative TPS

Constraints, W/cm^2		No limit	681	568	454	397
SLA-561	Insulation thickness, cm	4.23	4.19	4.10	3.89	3.70
	Recession thickness, cm	9.99	10.04	10.71	11.44	11.83
	Total thickness, cm	14.22	14.23	14.81	15.33	15.53
AVCOAT-5026	Insulation thickness, cm	4.94	4.90	4.81	4.61	4.42
	Recession thickness, cm	11.29	11.35	12.12	12.95	13.38
	Total thickness, cm	16.23	16.25	16.93	17.56	17.80

Table 9 Area definition of TPS for different heating rate limits

Constraints, W/cm^2	No limit	681	568	454	397
Ablative material, m^2	13.73	11.44	7.72	5.22	4.17
Reusable material, m^2	28.76	31.05	34.77	37.27	38.32

Table 10 TPS mass of SLA-561 for different heating rate limits

Constraints, W/cm^2	No limit	681	568	454	397
SLA-561, kg	52.8	49.1	43.8	39.5	37.2
LI-900, kg	59.4	64.6	75.7	77.3	78.1
Total TPS [a], kg	410.8	412.4	418.3	415.5	413.9

[a]Including support structure.

Table 11 TPS mass of AVCOAT-5026 for different heating rate limits

Constraints, W/cm^2	No limit	681	568	454	397
AVCOAT-5026, kg	120.6	112.0	99.4	88.6	82.5
LI-900, kg	59.4	64.6	75.7	77.3	78.1
Total TPS [a], kg	478.7	475.3	473.9	464.6	459.3

[a]Including support structure.

ablative material, the trend is different. This is because the area using the ablative material significantly reduces as the heat limit gets lower. Consequently, the total mass of the TPS, including masses of ablative material, LI-900, and support structure, does not vary much with respect to the total heat load, even though the maximum required thicknesses for each section varies significantly.

Tables 12 and 13 show the mass gain for each case. The amount of fuel saving is obtained by comparing the original fuel carrying capacity, 2702.8 kg (Table 1), to the required fuel consumption for the inclination change, and the total mass gain is calculated by subtracting the TPS mass from the fuel saving. This mass gain is equivalent to additional available payload mass because we have made the assumption that the total weight and the exterior shape of the vehicle are fixed.

The total mass gain for the best case (no limit case) is about 600 kg compared to that of the all-propulsive maneuver. This means that, even when considering the mass penalty induced by the TPS requirement, the aeroassisted maneuver still presents a substantial mass advantage over an all-propulsive maneuver. In addition, when designing the lightest vehicle with a fixed payload mass, the mass gain will be amplified. The mass saving, especially in fuel consumption, would bring a further mass reduction because it would allow for a smaller vehicle that requires less vehicle structure and TPS, thus bringing the total mass further down.

Note also that we used a relatively simple TPS mass estimation model that we tried to make conservative. The main conservative assumptions are as follows: neglecting the insulation role of the recession thickness in the virtual ablation method, assuming that the heating rate distribution over the vehicle length does not vary along the vehicle width (in reality the heating rate decreases toward the tip of the wings), and assuming the heating rate distribution is

Table 12 Mass gain with SLA-561 + LI-900 TPS

Constraints, W/cm^2	No limit	681	568	454	397	All propulsive
Fuel saving, kg	1075.2	1070.7	1007.5	801.0	613.9	0
Total TPS mass, kg	410.8	412.4	418.3	415.5	413.9	0
Total mass gain, kg	664.4	658.3	589.2	385.5	200.0	0

Table 13 Mass gain with AVCOAT-5026 + LI-900 TPS

Constraints, W/cm^2	No limit	681	568	454	397	All propulsive
Fuel saving, kg	1075.2	1070.7	1007.5	801.0	613.9	0
Total TPS mass, kg	478.7	475.3	473.9	464.6	459.3	0
Total mass gain, kg	596.5	595.4	533.6	336.4	154.6	0

independent of the angle of attack (the distribution used is for high angle of attack involving high heating). The main remaining unconservative assumptions include neglecting the radiative heat flux contribution and neglecting the leeward side TPS. Accordingly, the exact TPS mass, and so the corresponding mass savings, might change if a detailed TPS sizing analysis was carried out.

Two assumptions may have limited the fuel savings. First, the inclination change was done entirely via the aeroassist, without any propulsive inclination change. For low heating rate constraints, it is probably more efficient to have a propulsive inclination change at deorbit. For more details on this assumption, see Appendix B. Second, the coupling between the trajectory optimization and the TPS design was limited to a single parameter: the heat rate constraint. Because the mass of the TPS also depends on the total heat load, further savings may be realized by using a two-parameter coupling with both heat rate and total heat load constraints. For the present example, we do not expect that this second parameter will contribute much to the mass savings; however, for other vehicles, a two-parameter coupling may be beneficial.

VI. Conclusions

This article presented a mass tradeoff for an aeroassisted orbital transfer vehicle including both fuel mass and thermal protection system mass. For an aeroglide maneuver, we analyzed the effect of the coupling between the trajectory optimization and the thermal protection system size through a single coupling parameter: a maximum heating rate constraint. We considered a one-way coupling, assuming that the total weight and the exterior shape of the vehicle are fixed, which allowed us to construct a simple sequential MDO framework. We first carried out trajectory optimization that optimized all guidance-related parameters along the trajectory, including deorbit, boost, and recircularization impulses to determine the heating rate profiles for the different maximum heating rate constraints. Then, in a second step, a simplified mass estimation model was used to size the TPS for each heating rate profile. This model selected for the vehicle surface ablative or reusable materials according to the heating rate at the surface location. The reusable TPS section was then sized using a transient heat-transfer finite element model. The ablative TPS section was sized using the virtual ablation method.

It was found that, even when considering the TPS mass, an aeroassisted maneuver maintains a mass advantage over an all-propulsive maneuver. Remarkably, the total TPS mass was found to vary relatively little with the heating rate constraint compared to fuel saving variations. Accordingly, the minimum mass AOTV (including both fuel and TPS masses) was found to be achieved if no heating rate constraint was imposed, which is also the scenario that minimizes the fuel consumption alone. The presented MDO framework is general and can potentially be applied to different vehicles, aeroassisted orbital transfer scenarios, or TPS mass estimation models, as long as the assumption is made that the achieved mass savings are transformed into additional payload capacity so that the total mass and shape of the vehicle remain constant.

Appendix A: Optimal Control of Trajectory Optimization

Examining the detail of the trajectories, Table A1 shows details of these trajectories, such as the initial velocity v_i, initial flight-path angle γ_i, final velocity v_e, final flight-path angle γ_e, and maximum velocity during the descent phase $v_{\max}$. Figures A1–A3 show the profile of the control variables, angle of attack α, and bank angle σ. A slightly steeper initial flight-path angle is applied to the most constrained case, the 397 W/cm^2 case. As discussed earlier, the magnitude of v_e mainly has an effect on fuel saving. Accordingly, what is important during the descent phase is to increase its velocity as much as possible before the inclination change phase, where the velocity significantly decreases due to the dense atmospheric drag. A

Table A1 Details of aeroglide trajectories

$\dot{Q}_{\max}$, W/cm^2	γ_i, deg	v_i, m/s	γ_e, deg	v_e, m/s	$v_{\max}$, m/s
397	−0.523	7827.3	0	6204.4	7879.8
454	−0.482	7830.2	0	6398.1	7880.8
568	−0.442	7832.7	0	6598.6	7878.1
681	−0.419	7834.1	0	6656.7	7876.9
No limit	−0.416	7834.3	1.6×10^{-3}	6660.8	7877.6

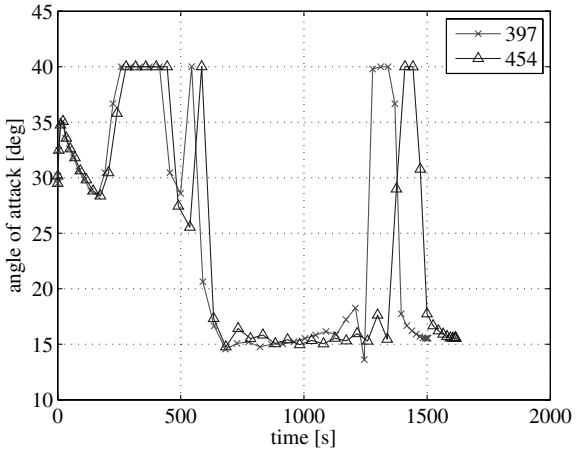

Fig. A1 Angle of attack vs time (1/2).

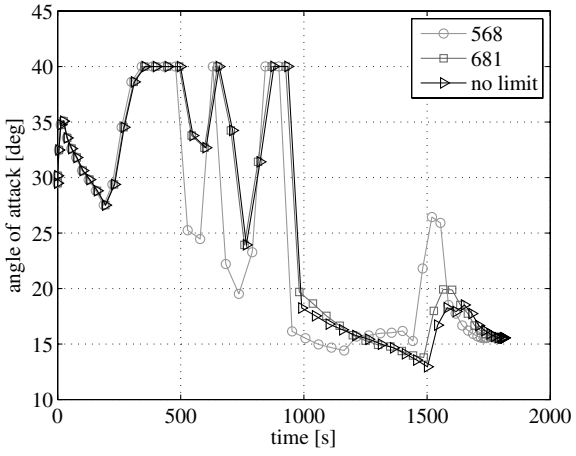

Fig. A2 Angle of attack vs time (2/2).

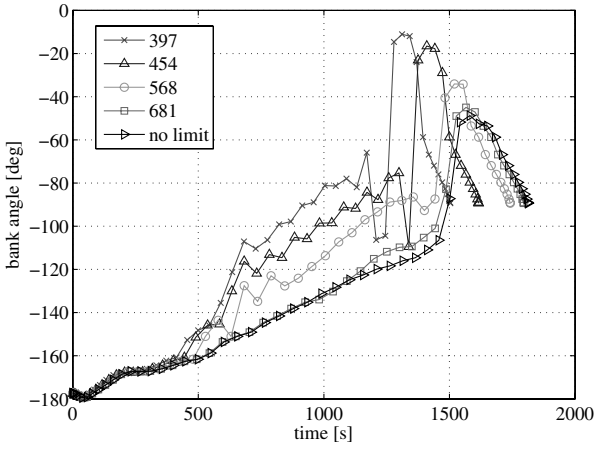

Fig. A3 Bank angle vs time.

Table B1 Solutions with propulsive inclination change at deorbit (with AVCOAT)

$\dot{Q}_{max}$, W/cm^2	Fuel consumption, kg	TPS mass, kg	Total heat load, J/cm^2	Fuel, kg	Deorbit inclination change, deg
284	2500.1	379.0	125,250	1787.2	10.2
341	2311.2	396.8	132,410	1274.4	6.7
397	2064.5	440.0	158,870	427.5	2.0
454	1862.1	469.0	171,200	103.5	0.4
568	1688.6	474.4	160,140	56.7	0.1
681	1629.6	474.1	149,820	50.2	0.1
No limit	1627.6	480.8	148,910	46.0	0.0

steeper flight can take advantage of using gravity efficiently to increase the velocity during the descent phase, even though a steeper initial flight-path angle increases fuel consumption due to a larger deorbit impulse and a smaller initial entry velocity, according to Kepler's laws of planetary motion. Indeed, for the 397 W/cm^2 case, the most velocity losing case, the steepest flight-path angle contributes to maintaining the velocity more in the descent phase as shown by v_{max}.

In all cases, the atmospheric flight starts with an angle of attack of about 35 deg and a bank angle of about −180 deg. At the beginning of the descent phase where the air density is quite small, a high angle of attack and a bank angle of about −180 deg are needed to generate a downward force to decrease the altitude. During the descent phase, it can be seen that the angle of attack varies actively. Generally, in terms of maintaining the velocity, reducing the angle of attack with decreasing altitude is preferable because a high angle of attack also leads to a high drag force. On the other hand, generating as large a lateral force as possible by combining a high angle of attack with a certain bank angle is needed to achieve the desired inclination change quickly. The jaggedness of the angle of attack in the numerical solution is most likely due to this tradeoff. This behavior is numerical noise because the air density in the descent phase is too small to generate a meaningful aerodynamic force. (In other words, the behavior of the angle of attack has to be big to generate a significant aerodynamic force in such a thin atmosphere.)

Once the altitude decreases enough to get a sufficient aerodynamic force to change the inclination (at an altitude of around 70 km), the angle of attack remains at around 16 deg, which corresponds to the maximum L/D. It allows the vehicle to fly as efficiently as possible without losing its velocity excessively because, in this altitude region, the drag force is not negligible. As the altitude approaches its minimum, where the vehicle meets maximum aerodynamic forces and correspondingly maximum heating rates, the bank angle gets close to −90 deg to generate the maximum lateral force to make the inclination change. After the desired inclination is achieved, to go back to the initial orbit altitude, the upward force is created by taking the highest angle of attack and a bank angle of close to 0 deg.

Appendix B: Solutions with Deorbit Inclination Change

To get the solution with an inclination change at deorbit, the restraint on the deorbit impulse ΔV_1, which is fixed in the equatorial plane, is removed. The TPS thickness for the insulation thickness of ablative material and LI-900 are easily modified by using the fact that TPS thicknesses are approximately linear in the total heat load. The other parts of the trajectory optimization and TPS mass estimation are repeated by the procedure previously described in this paper. Table B1 shows the fuel consumption, the total TPS mass, the total heat load, and the inclination change at deorbit.

For the higher heating rate constraint cases (i.e., no limit, 681, and 568 W/cm^2 cases), the fuel consumptions and TPS masses are almost the same as the original case (Tables 5 and 11) because the inclination changes achieved at deorbit are almost zero. It is also evident that, for high heat rate constraints, the aeroassisted maneuver is again significantly more advantageous in terms of fuel saving compared to the all-propulsive maneuver. As the heating rate constraint gets lower (454 and 397 W/cm^2 cases), the lowest fuel consumption is achieved with small inclination change at deorbit. For even lower heat constraints, the aeroassist maneuver is not reasonable because the capability of the aerodynamic inclination change is limited and, also, a large amount of inclination change at deorbit is required. In addition to the large fuel consumption, a TPS which is not negligible in terms of mass is still required.

References

[1] Stephen, A. W., and Bonnie, J. D., "Orbital Space Plane, Past, Present, and Future," AIAA Paper 2003-2718, July 2003.

[2] Walberg, G. D., "A Survey of Aeroassisted Orbit Transfer," *Journal of Spacecraft and Rockets*, Vol. 22, No. 1, 1985, pp. 3–18. doi:10.2514/3.25704

[3] Mease, K. D., "Optimization of Aeroassisted Orbital Transfer: Current Status," *Journal of the Astronautical Sciences*, Vol. 36, Nos. 1–2, 1988, pp. 7–33.

[4] Lee, J. Y., and Hull, D. G., "Maximum Orbit Plane Change with Heat-Transfer-Rate Considerations," *Journal of Guidance, Control, and Dynamics*, Vol. 13, No. 3, 1990, pp. 492–497. doi:10.2514/3.25362

[5] Seywald, H., "Optimal Control Solutions for an Aeroassisted Orbital Transfer Problem with a Heating Rate Limit," AIAA Paper 1994-3647, Aug. 1994.

[6] Zimmermann, F., and Calise, A. J., "Numerical Optimization Study of Aeroassisted Orbital Transfer," *Journal of Guidance, Control, and Dynamics*, Vol. 21, No. 1, 1998, pp. 127–133. doi:10.2514/2.4208

[7] Rao, A. V., Tang, S., and Hallman, W. P., "Numerical Optimization Study of Multiple-Pass Aeroassisted Orbital Transfer," *Optimal Control Applications and Methods*, Vol. 23, No. 4, July–Aug. 2002, pp. 215–238. doi:10.1002/oca.711

[8] Rehder, J. J., "Multiple Pass Trajectories for an Aeroassisted Orbital Transfer Vehicle," AIAA Paper 84-0407, Jan. 1984.

[9] Pienkowski, J., Whitmore, S., and Spencer, M., "Analysis of the Aerodynamic Orbital Transfer Capabilities of the X-37 Space Maneuvering Vehicle (SMV)," AIAA Paper 2003-908, Jan. 2003.

[10] Rao, A. V., "User's Manual for GPOCS Version 1.1: A MATLAB Implementation of the Gauss Pseudospectral Method," TOMLAB Optimization, Vasteras, Sweden, Sept. 2007.

[11] Benson, D. A., Huntington, G. T., Thorvaldsen, T. P., and Rao, A. V., "Direct Trajectory Optimization and Costate Estimation via an Orthogonal Collocation Method," *Journal of Guidance, Control, and Dynamics*, Vol. 29, No. 6, Nov.–Dec. 2006, pp. 1435–1440. doi:10.2514/1.20478

[12] Ko, W. L., Gong, L., and Quinn, R. D., "Reentry Thermal Analysis of a Generic Crew Exploration Vehicle Structure," NASA TM-214607, 2007.

[13] Vinh, N-X, Busemann, A., and Culp, R. D., *Hypersonic and Planetary Entry Flight Mechanics*, Univ.of Michigan Press, Ann Arbor, MI, 1980, pp. 19–28.

[14] U.S. Standard Atmosphere, 1962, U.S. Government, Washington, D.C., 1962.

[15] Detra, R. W., Kemp, N. N., and Riddell, F. R., "Addendum to 'Heat Transfer to Satellite Vehicles Reentering the Atmosphere'," *Jet Propulsion*, Vol. 27, No. 12, 1957, pp. 1256–1257.

[16] Holmstrom, K., Goran, A. O., and Edvall, M. M., "User's Guide for TOMLAB/SNOPT," TOMLAB Optimization, 5 July 2005.

[17] Gill, P. E., Murray, W., and Saunders, M. A., "SNOPT: An SQP Algorithm for Large Scale Constrained Optimization," *SIAM Journal on Optimization*, Vol. 12, No. 4, 2002, pp. 979–1006. doi:10.1137/S1052623499350013

[18] Erb, R. B., Greenshields, D. H., Chauvin, L. T., and Pavlosky, J. E., "Apollo Thermal-Protection System Development," *Journal of Spacecraft and Rockets*, Vol. 7, No. 6, 1970, pp. 727–734. doi:10.2514/3.30027

[19] NASA Ames Thermal Protective Materials and System Branch, TPSX Database [online database], http://tpsx.arc.nasa.gov/index.html, 26 Sept. 2007.
[20] Williams, S. D., and Curry, D. M., "Thermal Protection Materials Thermophysical Property Data," NASA RP-1289, 1992.
[21] Menees, G. P., Brown, K. G., Wilson, J. F., and Davies, C. B., "Aerothermodynamic Heating and Performance Analysis of a High-Lift Aeromaneuvering AOTV Concept," *Journal of Spacecraft and Rockets*, Vol. 24, No. 3, 1987, pp. 198–204. doi:10.2514/3.25899
[22] NASA Marshall Space Flight Center, "NASA Facts," FS-2003-05-65-MSFC, May 2003.
[23] Myers, D., Martin, C., and Blosser, M. L., "Parametric Weight Comparison of Advanced Metallic, Ceramic Tile, and Ceramic Blanket Thermal Protection Systems (TPS)," NASA TM-210289, 2000.
[24] Olynick, D., Chen, Y. K., and Tauber, M. E., "Forebody TPS Sizing with Radiation and Ablation for the Stardust Sample Return Capsule," AIAA Paper 1997-2474, June 1997.
[25] Bartlett, E. P., Abbett, M. J., Nicolet, W. E., and Moyer, C. B., "Improved Heat-Shield Design Procedures for Manned Entry Systems, Part II: Application to Apollo," NASA CR-108689, 1970.
[26] "Postlaunch Report for Mission AS-202 (Apollo Spacecraft 011)," NASA Manned Spacecraft Center Rept. MSC-A-R-66-5, Oct. 1966.